Research Article Vol. 8, No. 4 / April 2021 / Optica 539

Ultralow-threshold thin-film lithium niobate optical parametric oscillator

Juanjuan Lu,[1] Ayed Al Sayem,[1] Zheng Gong,[1] Joshua B. Surya,[1] Chang-Ling Zou,[2] and Hong X. Tang[1,*]

[1]Department of Electrical Engineering, Yale University, New Haven, Connecticut 06511, USA
[2]Department of Optics, University of Science and Technology of China, Hefei 230026, China
*Corresponding author: hong.tang@yale.edu

Received 4 January 2021; revised 17 March 2021; accepted 24 March 2021 (Doc. ID 418984); published 12 April 2021

Materials with strong second-order ($\chi^{(2)}$) optical nonlinearity, especially lithium niobate, play a critical role in building optical parametric oscillators (OPOs). However, chip-scale integration of low-loss $\chi^{(2)}$ materials remains challenging and limits the threshold power of on-chip $\chi^{(2)}$ OPO. Here we report an on-chip lithium niobate optical parametric oscillator at the telecom wavelengths using a quasi-phase-matched, high-quality microring resonator, whose threshold power (~30 μW) is 400 times lower than that in previous $\chi^{(2)}$ integrated photonics platforms. An on-chip power conversion efficiency of 11% is obtained from pump to signal and idler fields at a pump power of 93 μW. The OPO wavelength tuning is achieved by varying the pump frequency and chip temperature. With the lowest power threshold among all on-chip OPOs demonstrated so far, as well as advantages including high conversion efficiency, flexibility in quasi-phase-matching, and device scalability, the thin-film lithium niobate OPO opens new opportunities for chip-based tunable classical and quantum light sources and provides a potential platform for realizing photonic neural networks. © 2021 Optical Society of America under the terms of the OSA Open Access Publishing Agreement

https://doi.org/10.1364/OPTICA.418984

1. INTRODUCTION

Second-order-nonlinearity ($\chi^{(2)}$)-based optical parametric oscillators (OPOs) are critical sources of coherent radiation over a wide spectral range and have been workhorses for spectroscopy in the near- and mid-infrared regimes [1–3]. They are also widely used as non-classic light sources for applications in quantum information processing, including quantum random number generation, quantum key distribution, and recently demonstrated Ising machines [4–7]. Microcavity-based OPO has been particularly attractive due to its miniaturization and power efficiency. With ultrahigh optical quality (Q) factor of 10^7-10^8 afforded by the whispering-gallery-resonator (WGR) system, low-threshold OPOs have been achieved in various bulk WGRs [8–14], especially the highly polished lithium niobate (LN) WGRs with $\chi^{(2)}$ nonlinearity.

Over the past decade, the demand for scalability in photonic components has stimulated efforts to produce on-chip OPO via the $\chi^{(2)}$ nonlinearity [15], however, whose threshold power is tens of milliwatts and remains orders of magnitude larger than state-of-the-art value (6.7 μW) of lithium niobate WGR [10]. Hence, low-threshold and scalable $\chi^{(2)}$ OPO remains challenging. Recently, thin-film LN has emerged as a compelling integrated nonlinear and quantum photonics platform whose favorable performances, including electro-optic modulation [16–18], supercontinuum generation [19,20], Kerr frequency comb generation [21,22], frequency conversion [23–26], and entangled photon pair generation [27,28], have by now been well demonstrated.

In this Letter, we first demonstrate an ultralow-threshold, chip-integrated OPO using a periodically poled lithium niobate microring resonator (PPLNMR). With high optical confinement and strong spatial mode overlap via the quasi-phase-matching, a threshold power as low as 30 μW is demonstrated for the parametric oscillation at the infrared band, which is a state-of-the-art value reported among all current integrated photonics platforms. Meanwhile, an absolute power conversion efficiency of 11% is obtained for the combined signal and idler waves at a pump power of 93 μW. The OPO wavelength tuning is investigated by varying the pump frequency and chip temperature. A tuning bandwidth of 170 nm is addressed through a small change of 5 nm in pump wavelength. Alternatively, with a fixed pump mode, the temperature tuning is implemented for fine control of the signal and idler output wavelengths from a widely separated (230 nm) case to the degeneracy. Overall, low threshold, wide tunability, as well as flexibility in phase-matching by domain poling make thin-film LN OPO the ideal candidate for compact, versatile light sources for various on-chip optical applications such as sensing, frequency comb spectroscopy, and quantum squeezers.

2. DEVICE DESIGN AND FABRICATION

Figure 1(a) illustrates the principle of our lithium niobate microring OPO device, in which the $\chi^{(2)}$-based parametric down-conversion process allows the generation of the infrared signal and idler lights with a near-visible pump. $\omega_p/\omega_s/\omega_i$ represent

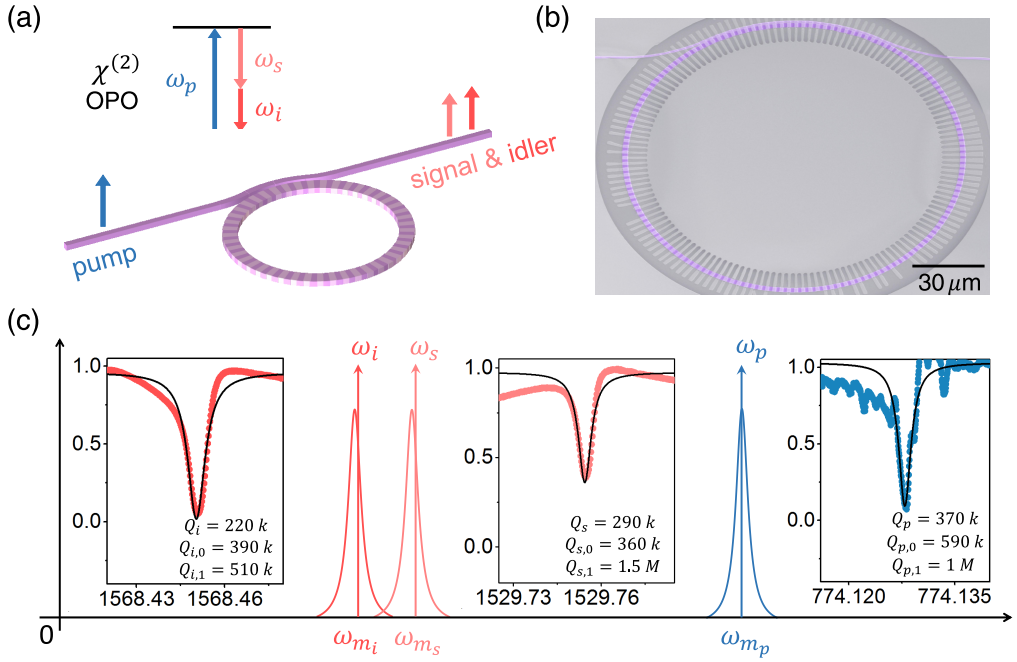

Fig. 1. Design and fabrication of a quasi-phase-matched optical parametric oscillator. (a) Illustration of the parametric oscillation using a $\chi^{(2)}$ PPLNMR. Signal and idler lights at the telecom wavelengths are generated by a near-visible pump. ω_p, ω_s, and ω_i represent frequencies for the pump, signal, and idler lights, respectively. (b) Scanning electron micrograph of a PPLNMR mock-up etched in hydrofluoric acid. (c) Schematics of the mode frequencies (denoted as ω_{m_i}, ω_{m_s}, and ω_{m_p}, respectively) and their respective transmission spectrum with the extracted Q values shown in the inset. The subscripts 0, 1 represent the intrinsic and coupling Q factors, respectively. The discrepancy between the photon and resonance frequencies is the frequency detuning, which could be written as $\delta_{p/s/i} = \omega_{p/s/i} - \omega_{m_{p/s/i}}$.

the pump/signal/idler photon frequencies with their energy conservation ($\omega_p = \omega_s + \omega_i$) shown in the inset. When the phase-matching and triply resonant conditions are satisfied for these three optical modes, the parametric process would be enhanced by the high-Q resonator. The theoretical pump power threshold P_{th} for parametric oscillation could be obtained when the optical loss and parametric gain are balanced [15]:

$$P_{\text{th}} = \frac{\hbar\omega_p}{8g^2}\frac{\kappa_s\kappa_i\kappa_p^2}{\kappa_{p,1}} = \frac{\hbar\omega_s\omega_i\omega_p^2}{64g^2}\frac{Q_{p,1}}{Q_sQ_iQ_p^2}, \tag{1}$$

where g is the vacuum coupling strength between the three interacting modes, $Q(\kappa)_{s/i/p}$ is their respective loaded Q factor (total dissipation rate), and $Q(\kappa)_{p,1}$ is the coupling Q factor (external dissipation rate) of the pump mode. Therefore, a large g and high Q factors are always beneficial to reduce the OPO threshold power.

In the microring resonator, the coupling rate g is dependent on the material $\chi^{(2)}$ coefficient and modal overlap factor γ through the relation $g \propto \chi^{(2)}\gamma$ [25]. Here, to optimize g, we utilize the largest $\chi^{(2)}$ tensor element d_{33} of z-cut LN thin film, and we also improve the mode overlap factor γ close to unity by employing fundamental transverse-magnetic (TM) modes. In contrast to previous study of on-chip OPO in an AlN platform [15], where the high-order mode is leveraged to compensate the dispersion at the visible wavelength, we realize the quasi-phase-matching (momentum conservation) between fundamental TM modes via the radial periodic poling of the LN microring. An azimuthal grating number $M = 146$ (poling period $\Lambda = 2\pi R/M = 3$ μm) is designed to compensate for the momentum mismatch $\Delta m = |m_s + m_i - m_p|$ for the parametric oscillation at 1550 nm with a pump at 775 nm (see Supplement 1, Section 1 for device design details). Figure 1(b) is a scanning electron micrograph of a fabricated PPLNMR mock-up etched in hydrofluoric acid, revealing a high-fidelity periodic domain poling (see Supplement 1, Section 2 for the fabrication details). The cavity transmission spectra of the signal, idler, and pump modes for the subsequent OPO are plotted in Fig. 1(c), where Lorentzian fittings are applied to extract loaded Q factors of 2.9×10^5, 2.2×10^5, and 3.7×10^5, respectively. Their intrinsic Q factors are calculated to be 3.6×10^5, 3.9×10^5, and 5.9×10^5 at under-coupled conditions, which are confirmed by measuring the dependence of loaded quality factor on the coupling gap in an array of fabricated devices.

3. RESULT AND DISCUSSION

When pumping the device by a near-visible tunable laser (New Focus TLB-6712, 766–781 nm), the parametric oscillation at the infrared wavelengths could be observed if the pump power exceeds the threshold. In practice, due to the frequency detunings induced during the fabrication process, as indicated in Fig. 1(c), the OPO threshold rises to $P_{\text{th}} \cdot (1 + \delta^2/\kappa_i\kappa_s)$ even for a resonant pump ($\omega_p = \omega_{m_p}$), with $\delta = \omega_{m_p} - \omega_{m_s} - \omega_{m_i}$ being the resonance frequency mismatch [29]. By controlling the chip temperature to adjust δ and varying the pump power, the parametric oscillation with the lowest threshold is observed when the device is pumped at the resonance near 774.1 nm at an optimal temperature of 125°C (see Supplement 1, Section 3 for the temperature optimization details). The measured on-chip OPO power P_{s+i} and absolute power conversion efficiency, defined as $\eta = P_{s+i}/P_p$, are plotted against the on-chip pump power with the red circles and asterisks in Figs. 2(a) and 2(b), respectively. A threshold power P_{th} of 30 ± 1.5 μW is identified and corresponds to an intracavity

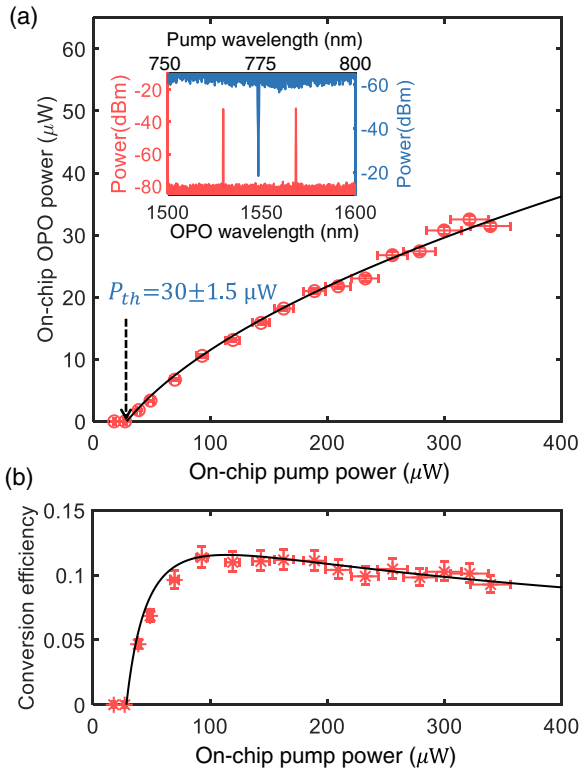

Fig. 2. Power dependence of the PPLNMR-based OPO. (a) The experimental (red circles) and theoretical (solid line) on-chip infrared power versus on-chip pump power for the parametric oscillation process. An example snapshot of off-chip pump (blue) and parametric oscillation (red) spectra after the device are shown in the inset. (b) On-chip conversion efficiency of pump to both signal and idler fields versus pump power, where a theoretical fit (solid line) is applied. Error bars are deviations considering a coupling fluctuation of 2% and 5% for the respective infrared and near-visible light.

pump photon number of $\sim 5.4 \times 10^4$. The parametric oscillation spectrum at a pump power of 120 μW is recorded using an optical spectrum analyzer (Yokogawa AQ6374, 350–1750 nm), where distinct signal and idler waves are resolved at 1529.7 and 1568.4 nm, respectively, as shown in the inset. Based on the microring geometry, the azimuthal numbers of the corresponding pump, signal, and idler modes were respectively simulated to be $m_p = 1196$, $m_s = 534$, and $m_i = 516$, whose momentum mismatch is successfully compensated by a radial poling structure with $M = 146$ as designed. To capture the OPO spectrum, the laser-cavity locking is achieved by approaching the resonance from the red-detuned side, similar to the process discussed in Refs. [30,31]

Substituting the measured threshold and Q factors [Fig. 1(c)] in Eq. (1), we extract a $g/2\pi$ of 1.18 ± 0.03 MHz, consistent with the value obtained via the independent second-harmonic generation (SHG) measurement [26]. Theoretically, the power of the signal and idler OPO emission under the triply resonant condition could be derived as [15]

$$P_{s+i} = \left(\frac{2Q_s}{Q_{s,1}} + \frac{2Q_i}{Q_{i,1}}\right)\frac{Q_p}{Q_{p,1}} P_{\text{th}}\left(\sqrt{P_p/P_{\text{th}}} - 1\right). \quad (2)$$

The theoretical predictions (solid black lines) based on Eq. (2) are plotted in Figs. 2(a) and 2(b) and match well with the experimental data (red symbols). With an elevated on-chip near-visible pump power of 93.0 μW, we record an off-chip infrared power of 1.5 μW corresponding to an on-chip OPO power of 10.5 μW, which further translates to a conversion efficiency η of 11% [Fig. 2(b)]. According to Eq. (2), the conversion efficiency reaches its maximum on the condition that $P_p = 4P_{\text{th}}$, where $\eta_{\max} = (2Q_s/Q_{s,1} + 2Q_i/Q_{i,1})(Q_p/Q_{p,1})/4$. The efficiency depletion at the high-power regime is mainly attributed to the back-conversion of the signal and idler fields. Different coupling conditions could be adapted by varying the gap between the bus waveguide and microring for various applications. For example, a $\eta_{\max}$ of 0.25 is derived with the assumption that all three interacting modes are critical coupled, while a strong over-coupling condition provides a $\eta_{\max}$ approaching unity. In our case, the under-coupling condition provides an ultralow threshold of 30 μW, though it limits our current $\eta_{\max}$ to 11%. During the measurement, we observe that subsidiary peaks appear due to the cascaded second-order nonlinearity, and third-order nonlinear effect starts to kick in when we drive the device at higher pump powers. These lead to the power jump and Pockels microcomb generation due to the competing second- and third-order optical nonlinearities, which we are actively investigating and will be discussed in a future work.

We further verify the feasibility of our ultralow-threshold OPO in wavelength tuning over a large spectrum range, which promises flexible coherent optical sources for future on-chip applications. It is well known that, in the microring resonator, the phase-matching condition could be satisfied simultaneously by many signal-idler mode pairs, with their wavelength difference increasing at intervals of 2 times the free spectral range (FSR) for given pump mode and temperature. However, due to the inherent dispersion, the frequency mismatch δ varies for different mode pairs, and only one pair of modes oscillates with the lowest threshold. Therefore, we investigate the tuning of signal and idler wavelengths by varying the resonator temperature as well as the pump mode number.

As indicated by the solid colored lines in the middle panel of Fig. 3, the theory predicts that the quasi-phase-matched signal and idler wavelengths could be continuously tuned as a function of the pump wavelength and the chip temperature (see Supplement 1, Section 1 for the simulation details). However, due to the constraint of the resonant condition, we could only experimentally access discrete points on these lines as marked by the red circles. On the one hand, the pump wavelength tuning provides discrete and relatively large OPO tuning step limited by the FSR. For a given temperature, the spectral separation between the signal and idler increases with the decreasing pump wavelengths. As an example, by fixing the operation temperature at 125°C, the OPO wavelength could be tuned from 1460 to 1630 nm, with a pump wavelength change of 5 nm. The detailed spectra are plotted on the right panel, whose signal and idler wavelengths are mapped to the middle panel (red circles) and show good agreement with the theoretical predication (solid lines). On the other hand, precise wavelength tuning could be achieved by utilizing the thermo-optic effect of the LN microring. As indicated in the blue shaded region of Fig. 3, for a given pump mode, the thermal tuning allows for the fine control of the signal and idler wavelengths from a widely separated situation to the degeneracy. With a pump around 770.5 nm, the measured OPO spectra at various temperatures are plotted on the left panel. The signal and idler wavelengths are tuned from 1430 to 1670 nm by varying the temperature between 100°C and 140°C, including an degenerate case demonstrated at an optimal temperature around 140°C. Here the tuning range is mainly limited by the

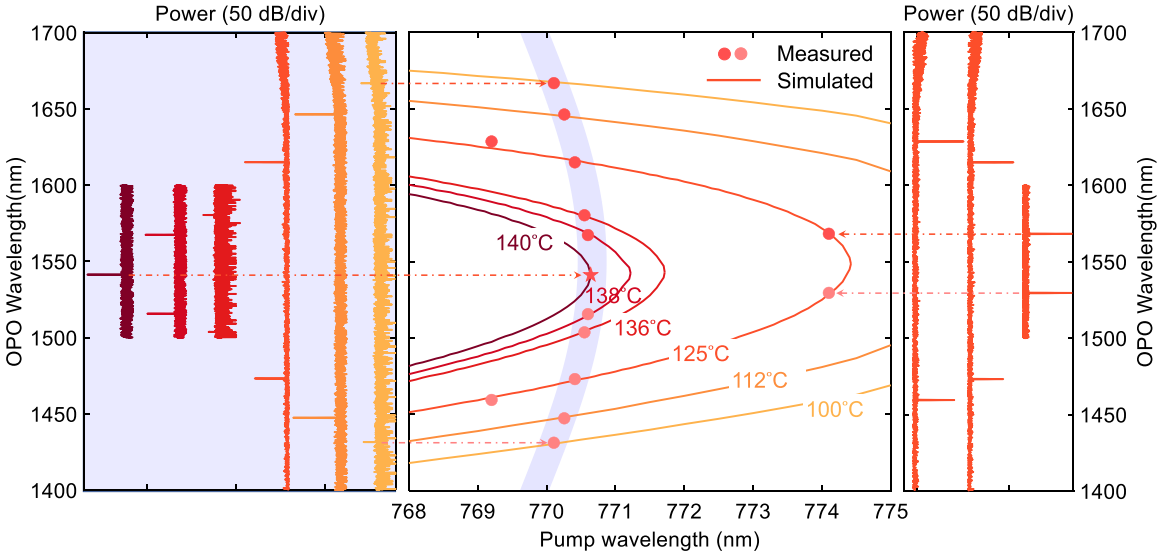

Fig. 3. OPO wavelength tuning by varying both the temperature and pump wavelength. Middle panel: simulated (solid lines) and measured (circles) OPO wavelengths versus the pump wavelength at various temperatures. As an example, the right panel plots the recorded spectra with different pump wavelengths at 125°C. The left panel indicates the occurrence of degenerate parametric oscillation by varying the temperature.

Table 1. Performances of Various Nonlinear Integrated Platforms for Microcavity-Enhanced Parametric Oscillation

Nonlinear Process	Materials	n_0	$\chi^{(3)}$ (10^{-18}m^2/W)	$\chi^{(2)}$ (pm/V)	$\lambda_p - \lambda_s - \lambda_i$ (nm)	Q ($\times 10^6$)	P_{th} (mW)	Ref.
$\chi^{(2)}$	LN	2.2	0.18	40	770–1430–1670	0.6	**0.030**	this work
	AlN	2.1	0.23	6	780–1480–1650	1.0	12	[15]
$\chi^{(3)}$	Si_3N_4	2	0.25	—	1560–1550–1570	13.8	0.073	[46]
					900–700–1400	2.5	0.90	[32]
	SiO_2	1.4	0.022	—	1550–1560–1570	100	0.050	[47]
					1549–1548–1550	1100	0.95	[48]
	Si	3.5	10	—	2600–2500–2700	0.6	3.1	[49]
	AlN	2.1	0.23	6	1560–1530–1590	1.6	25	[36]
	LN	2.2	0.18	40	1560–1540–1580	1.1	80	[21]
	GaP	3.1	11	82	1560–1540–1580	0.2	3.0	[50]
	AlGaAs	3.4	26	240	1540–1520–1560	1.5	0.036	[51]
	SiC	2.7	1	24	1560–1525–1595	1.1	8.5	[52]]

dispersion. In principle, it could be further extended by tailoring the device geometries for the dispersion engineering [32]. Overall, our OPO device has shown good potential to realize the relatively precise control of oscillation wavelengths over a broad range by combining pump wavelength and temperature tunings. Noting that the demonstrated wavelength tuning is broad but inherently discrete, continuous tuning (mode-hop free) is always demanding and remains to be investigated. The thermal tuning has proven to access tens of gigahertz (GHz) continuous tuning range [33]. By cascading multiple microrings with varying device geometries on one single bus waveguide [34,35], in cooperation with the thermal tuning, the ultimate tuning range of multiple resonators could possibly overlap and cover one single FSR continuously.

Finally, we compare the performances of various integrated platforms, including both the $\chi^{(2)}$ and $\chi^{(3)}$ mechanisms, for their respective state-of-the-art cavity-enhanced OPOs in terms of the material, refractive index n_0, nonlinear coefficients, device structure, operating wavelengths (extracted from the situation in which signal and idler have the widest separation), Q factor, and threshold power as presented in Table 1.

Theoretically, $P_{th} \propto 1/Q^2$ for the $\chi^{(3)}$ OPO [36]. However, in the case of the $\chi^{(2)}$ process, $P_{th} \propto 1/Q^3$ [Eq. (1)]. Therefore, to reach the same threshold, the $\chi^{(2)}$ OPO has a less stringent requirement on its Q factor. Despite the fact that silicon photonics, including Si, Si_3N_4, and SiO_2, have much higher Q factors due to their mature fabrication techniques, the demonstration in this work, to the best of our knowledge, delivers the lowest threshold power among all on-chip OPOs so far. Moreover, due to the three-wave-mixing nature, the $\chi^{(2)}$ OPO offers broader spectral separation between the pump and signal (idler) fields intrinsically, which promises for sufficient on-chip filtering. We note that piezoelectric III–V materials, such as Al(Ga)N, (Al)GaAs, and GaP, feature both significant $\chi^{(2)}$ and $\chi^{(3)}$ nonlinear coefficients, while relying on challenging waveguide geometrical engineering to achieve modal phase matching between fundamental and high-order modes, which limits their OPO performance as well as operation wavelengths. Overall, the periodically poled thin-film lithium niobate microresonator prove to be an efficient OPO with the lowest power threshold. In addition, due to its flexibility in ferroelectric domain control for quasi-phase-matching and greatly enhanced light–matter interaction afforded by its high effective $\chi^{(2)}$ nonlinearity and Q factor, our device on a integrated photonic chip opens new possibilities for various applications, and alternative device designs could be envisioned based on target

applications. Firstly, the PPLNMR device promises chip-based tunable classical and quantum light sources. For example, the poling grating number M could be tailored to realize parametric oscillation at the mid-infrared wavelengths for molecular spectroscopy [37]. Over-coupling the degenerate signal modes could lead to efficient on-chip squeezers, which play a crucial role in continuous variable quantum information processing [38]. Second, due to the multiple modes and nonlinear optical processes present in the same device, the OPO dynamics could be an indicator for novel physics of light–matter interactions in the microresonator [39]. For example, inspired by the recent demonstrations on AlN microrings [40] and LN WGRs [41,42], an ultra-efficient Pockels soliton microcomb could be foreseen in the same device with the efforts of coordinating its Kerr, quadratic, and photorefractive effects [31,43]. Lastly, by coupling several PPLNMRs, significant nonlinear interplay between the OPOs offers an platform for realizing photonic neural networks and Ising models, which find applications in artificial machine learning [44,45].

4. CONCLUSION

In conclusion, we demonstrate $\chi^{(2)}$ optical parametric oscillation in lithium niobate nanophotonics. Leveraging the high optical confinement as well as optimized quasi-phase-matching condition, an ultralow power threshold (30 μW) of optical parametric oscillation is obtained, and an on-chip conversion efficiency of 11% is measured with an on-chip pump power of 93 μW. The tunability of the OPO wavelengths is also investigated via the pump-wavelength and temperature tuning, and the experimental results indicate a wide tuning range. By further pushing the Q factor to that of bulk LN WGRs, approaching 10^8, a pump threshold down to several picowatts could be attainable in PPLNMR devices, allowing the study of OPO at a few-photon level and critical for the scalability of photonic quantum systems. In light of the most recent works on near-octave comb generation, efficient SHG, and bright photon pair generation, PPLNMR devices hold promise for chip-based tunable coherent light sources as well as the monolithic realization of nonlinear and quantum photonics.

Funding. U.S. Department of Energy (DE-SC0019406); National Science Foundation (EFMA-1640959); David and Lucile Packard Foundation (2009-34719).

Acknowledgment. The facilities used for device fabrication were supported by the Yale SEAS cleanroom and Yale Institute for Nanoscience and Quantum Engineering. The authors thank Dr. Michael Rooks, Dr. Yong Sun, Sean Rinehart, and Kelly Woods for assistance in device fabrication.

Disclosures. The authors declare no conflicts of interest.

Data Availability. The data that support the findings of this study are available from the corresponding authors upon reasonable request.

Supplemental document. See Supplement 1 for supporting content.

REFERENCES

1. M. H. Dunn and M. Ebrahimzadeh, "Parametric generation of tunable light from continuous-wave to femtosecond pulses," Science **286**, 1513–1517 (1999).
2. D. D. Arslanov, M. Spunei, J. Mandon, S. M. Cristescu, S. T. Persijn, and F. J. M. Harren, "Continuous-wave optical parametric oscillator based infrared spectroscopy for sensitive molecular gas sensing," Laser Photon. Rev. **7**, 188–206 (2013).
3. L. Maidment, P. G. Schunemann, and D. T. Reid, "Molecular fingerprint-region spectroscopy from 5 to 12 μm using an orientation-patterned gallium phosphide optical parametric oscillator," Opt. Lett. **41**, 4261–4264 (2016).
4. U. L. Andersen, T. Gehring, C. Marquardt, and G. Leuchs, "30 years of squeezed light generation," Phys. Scripta **91**, 053001 (2016).
5. L. S. Madsen, V. C. Usenko, M. Lassen, R. Filip, and U. L. Andersen, "Continuous variable quantum key distribution with modulated entangled states," Nat. Commun. **3**, 1083 (2012).
6. T. Inagaki, K. Inaba, R. Hamerly, K. Inoue, Y. Yamamoto, and H. Takesue, "Large-scale ising spin network based on degenerate optical parametric oscillators," Nat. Photonics **10**, 415–419 (2016).
7. Y. Yamamoto, K. Aihara, T. Leleu, K.-i. Kawarabayashi, S. Kako, M. Fejer, K. Inoue, and H. Takesue, "Coherent Ising machines—optical neural networks operating at the quantum limit," npj Quantum Inf. **3**, 49 (2017).
8. T. J. Kippenberg, S. M. Spillane, and K. J. Vahala, "Kerr-nonlinearity optical parametric oscillation in an ultrahigh-Q toroid microcavity," Phys. Rev. Lett. **93**, 083904 (2004).
9. A. A. Savchenkov, A. B. Matsko, D. Strekalov, M. Mohageg, V. S. Ilchenko, and L. Maleki, "Low threshold optical oscillations in a whispering gallery mode CaF_2 resonator," Phys. Rev. Lett. **93**, 243905 (2004).
10. J. U. Fürst, D. V. Strekalov, D. Elser, A. Aiello, U. L. Andersen, C. Marquardt, and G. Leuchs, "Low-threshold optical parametric oscillations in a whispering gallery mode resonator," Phys. Rev. Lett. **105**, 263904 (2010).
11. T. Beckmann, H. Linnenbank, H. Steigerwald, B. Sturman, D. Haertle, K. Buse, and I. Breunig, "Highly tunable low-threshold optical parametric oscillation in radially poled whispering gallery resonators," Phys. Rev. Lett. **106**, 143903 (2011).
12. S. J. Herr, C. S. Werner, K. Buse, and I. Breunig, "Quasi-phase-matched self-pumped optical parametric oscillation in a micro-resonator," Opt. Express **26**, 10813–10819 (2018).
13. N. L. B. Sayson, T. Bi, V. Ng, H. Pham, L. S. Trainor, H. G. Schwefel, S. Coen, M. Erkintalo, and S. G. Murdoch, "Octave-spanning tunable parametric oscillation in crystalline Kerr microresonators," Nat. Photonics **13**, 701–706 (2019).
14. S.-K. Meisenheimer, J. U. Fürst, K. Buse, and I. Breunig, "Continuous-wave optical parametric oscillation tunable up to an 8 μm wavelength," Optica **4**, 189–192 (2017).
15. A. W. Bruch, X. Liu, J. B. Surya, C.-L. Zou, and H. X. Tang, "On-chip $\chi^{(2)}$ microring optical parametric oscillator," Optica **6**, 1361–1366 (2019).
16. C. Wang, M. Zhang, X. Chen, M. Bertrand, A. Shams-Ansari, S. Chandrasekhar, P. Winzer, and M. Lončar, "Integrated lithium niobate electro-optic modulators operating at CMOS-compatible voltages," Nature **562**, 101–104 (2018).
17. M. Zhang, B. Buscaino, C. Wang, A. Shams-Ansari, C. Reimer, R. Zhu, J. M. Kahn, and M. Lončar, "Broadband electro-optic frequency comb generation in a lithium niobate microring resonator," Nature **568**, 373–377 (2019).
18. M. Li, J. Ling, Y. He, U. A. Javid, S. Xue, and Q. Lin, "Lithium niobate photonic-crystal electro-optic modulator," Nat. Commun. **11**, 4123 (2020).
19. J. Lu, J. B. Surya, X. Liu, Y. Xu, and H. X. Tang, "Octave-spanning supercontinuum generation in nanoscale lithium niobate waveguides," Opt. Lett. **44**, 1492 (2019).
20. Y. Okawachi, M. Yu, B. Desiatov, B. Y. Kim, T. Hansson, M. Lončar, and A. L. Gaeta, "Chip-based self-referencing using integrated lithium niobate waveguides," Optica **7**, 702–707 (2020).
21. C. Wang, M. Zhang, M. Yu, R. Zhu, H. Hu, and M. Loncar, "Monolithic lithium niobate photonic circuits for Kerr frequency comb generation and modulation," Nat. Commun. **10**, 978 (2019).
22. Z. Gong, X. Liu, Y. Xu, and H. X. Tang, "Near-octave lithium niobate soliton microcomb," Optica **7**, 1275–1278 (2020).
23. C. Wang, C. Langrock, A. Marandi, M. Jankowski, M. Zhang, B. Desiatov, M. M. Fejer, and M. Lončar, "Ultrahigh-efficiency wavelength conversion in nanophotonic periodically poled lithium niobate waveguides," Optica **5**, 1438 (2018).
24. J.-Y. Chen, Z.-H. Ma, Y. M. Sua, Z. Li, C. Tang, and Y.-P. Huang, "Ultra-efficient frequency conversion in quasi-phase-matched lithium niobate microrings," Optica **6**, 1244–1245 (2019).
25. J. Lu, J. B. Surya, X. Liu, A. W. Bruch, Z. Gong, Y. Xu, and H. X. Tang, "Periodically poled thin film lithium niobate microring resonators with a second-harmonic generation efficiency of 250,000%/W," Optica **6**, 1455–1460 (2019).

26. J. Lu, M. Li, C.-L. Zou, A. A. Sayem, and H. X. Tang, "Toward 1% single-photon anharmonicity with periodically poled lithium niobate microring resonators," Optica **7**, 1654–1659 (2020).
27. J. Zhao, C. Ma, M. Rüsing, and S. Mookherjea, "High quality entangled photon pair generation in periodically poled thin-film lithium niobate waveguides," Phys. Rev. Lett. **124**, 163603 (2020).
28. Z. Ma, J.-Y. Chen, Z. Li, C. Tang, Y. M. Sua, H. Fan, and Y.-P. Huang, "Ultrabright quantum photon sources on chip," Phys. Rev. Lett. **125**, 263602 (2020).
29. I. Breunig, "Three-wave mixing in whispering gallery resonators," Laser Photon. Rev. **10**, 569–587 (2016).
30. X. Sun, H. Liang, R. Luo, W. C. Jiang, X.-C. Zhang, and Q. Lin, "Nonlinear optical oscillation dynamics in high-Q lithium niobate microresonators," Opt. Express **25**, 13504–13516 (2017).
31. Y. He, Q.-F. Yang, J. Ling, R. Luo, H. Liang, M. Li, B. Shen, H. Wang, K. Vahala, and Q. Lin, "Self-starting bi-chromatic $LiNbO_3$ soliton microcomb," Optica **6**, 1138–1144 (2019).
32. X. Lu, G. Moille, A. Singh, Q. Li, D. A. Westly, A. Rao, S.-P. Yu, T. C. Briles, S. B. Papp, and K. Srinivasan, "Milliwatt-threshold visible–telecom optical parametric oscillation using silicon nanophotonics," Optica **6**, 1535–1541 (2019).
33. X.-X. Hu, J.-Q. Wang, Y.-H. Yang, J. B. Surya, Y.-L. Zhang, X.-B. Xu, M. Li, C.-H. Dong, G.-C. Guo, H. X. Tang, and C.-L. Zou, "All-optical thermal control for second-harmonic generation in an integrated microcavity," Opt. Express **28**, 11144–11155 (2020).
34. X. Guo, C.-L. Zou, H. Jung, Z. Gong, A. Bruch, L. Jiang, and H. X. Tang, "Efficient generation of a near-visible frequency comb via cherenkov-like radiation from a Kerr microcomb," Phys. Rev. Appl. **10**, 014012 (2018).
35. J. B. Surya, X. Guo, C.-L. Zou, and H. X. Tang, "Control of second-harmonic generation in doubly resonant aluminum nitride microrings to address a rubidium two-photon clock transition," Opt. Lett. **43**, 2696–2699 (2018).
36. X. Liu, C. Sun, B. Xiong, L. Wang, J. Wang, Y. Han, Z. Hao, H. Li, Y. Luo, J. Yan, T. Wei, Y. Zhang, and J. Wang, "Integrated high-Q crystalline AlN microresonators for broadband Kerr and Raman frequency combs," ACS Photon. **5**, 1943–1950 (2018).
37. F. K. Tittel, D. Richter, and A. Fried, "Mid-infrared laser applications in spectroscopy," in *Solid-State Mid-Infrared Laser Sources* (Springer, 2003), pp. 458–529.
38. Y. Zhao, Y. Okawachi, J. K. Jang, X. Ji, M. Lipson, and A. L. Gaeta, "Near-degenerate quadrature-squeezed vacuum generation on a silicon-nitride chip," Phys. Rev. Lett. **124**, 193601 (2020).
39. M. Li, C.-L. Zou, C.-H. Dong, X.-F. Ren, and D.-X. Dai, "Enhancement of second-harmonic generation based on the cascaded second- and third-order nonlinear processes in a multimode optical microcavity," Phys. Rev. A **98**, 013854 (2018).
40. A. W. Bruch, X. Liu, Z. Gong, J. B. Surya, M. Li, C.-L. Zou, and H. X. Tang, "Pockels soliton microcomb," Nat. Photonics **15**, 21–27 (2020).
41. J. Szabados, D. N. Puzyrev, Y. Minet, L. Reis, K. Buse, A. Villois, D. V. Skryabin, and I. Breunig, "Frequency comb generation via cascaded second-order nonlinearities in microresonators," Phys. Rev. Lett. **124**, 203902 (2020).
42. I. Hendry, L. S. Trainor, Y. Xu, S. Coen, S. G. Murdoch, H. G. L. Schwefel, and M. Erkintalo, "Experimental observation of internally pumped parametric oscillation and quadratic comb generation in a (2) whispering-gallery-mode microresonator," Opt. Lett. **45**, 1204–1207 (2020).
43. J. B. Surya, J. Lu, Y. Xu, and H. X. Tang, "Stable tuning of photorefractive microcavities using an auxiliary laser," Opt. Lett. **46**, 328–331 (2021).
44. J. Feldmann, N. Youngblood, C. D. Wright, H. Bhaskaran, and W. H. P. Pernice, "All-optical spiking neurosynaptic networks with self-learning capabilities," Nature **569**, 208–214 (2019).
45. Y. Yamamoto, T. Leleu, S. Ganguli, and H. Mabuchi, "Coherent Ising machines–quantum optics and neural network perspectives," Appl. Phys. Lett. **117**, 160501 (2020).
46. X. Ji, J. K. Jang, U. D. Dave, M. Corato-Zanarella, C. Joshi, A. L. Gaeta, and M. Lipson, "Exploiting ultralow loss multimode waveguides for broadband frequency combs," Laser Photon. Rev. **15**, 2000353 (2021).
47. P. Del'Haye, A. Schliesser, O. Arcizet, T. Wilken, R. Holzwarth, and T. J. Kippenberg, "Optical frequency comb generation from a monolithic microresonator," Nature **450**, 1214–1217 (2007).
48. L. Wu, H. Wang, Q. Yang, Q.-X. Ji, B. Shen, C. Bao, M. Gao, and K. Vahala, "Greater than one billion Q factor for on-chip microresonators," Opt. Lett. **45**, 5129–5131 (2020).
49. A. G. Griffith, R. K. Lau, J. Cardenas, Y. Okawachi, A. Mohanty, R. Fain, Y. H. D. Lee, M. Yu, C. T. Phare, C. B. Poitras, A. L. Gaeta, and M. Lipson, "Silicon-chip mid-infrared frequency comb generation," Nat. Commun. **6**, 6299 (2015).
50. D. J. Wilson, K. Schneider, S. Hönl, M. Anderson, Y. Baumgartner, L. Czornomaz, T. J. Kippenberg, and P. Seidler, "Integrated gallium phosphide nonlinear photonics," Nat. Photonics **14**, 57–62 (2020).
51. L. Chang, W. Xie, H. Shu, Q.-F. Yang, B. Shen, A. Boes, J. D. Peters, W. Jin, C. Xiang, S. Liu, G. Moille, S.-P. Yu, X. Wang, K. Srinivasan, S. B. Papp, K. Vahala, and J. E. Bowers, "Ultra-efficient frequency comb generation in AlGaAs-on-insulator microresonators," Nat. Commun. **11**, 1331 (2020).
52. M. A. Guidry, K. Y. Yang, D. M. Lukin, A. Markosyan, J. Yang, M. M. Fejer, and J. Vučković, "Optical parametric oscillation in silicon carbide nanophotonics," Optica **7**, 1139–1142 (2020).

128.36.7.169 {ts '2022-01-29 17:43:16'}